Dispersion-Engineered Guided-Wave Resonators in Anisotropic Single-Crystal Substrates—Part II: Numerical and Experimental Characterization

Mayur Ghatge, *Student Member, IEEE*, Mehrdad Ramezani, *Student Member, IEEE*, and Roozbeh Tabrizian, *Member, IEEE*

***Abstract*— In this part of the paper, the numerical and experimental verification of the analytical design procedure is presented. Various waveguide-based test vehicles, implemented in single-crystal silicon and transduced by thin aluminum nitride films, are demonstrated. Silicon resonators with type-I and type-II dispersion characteristics are presented to experimentally verify the analytical mode synthesis technique for realization of high-quality-factor silicon guided wave resonators.**

***Index Terms*— Acoustic energy localization, anisotropic single-crystal substrate, dispersion engineering, high-Q, Lamb wave dispersion, micromechanical resonator.**

I. Numerical Analysis of Vibration Modes

TO VERIFY the effectiveness of dispersion engineering for energy localization of guided waves in single-crystal anisotropic materials, analytically designed resonators with dispersion types I and II are simulated using COMSOL Multiphysics finite-element modeling (FEM) software. Table I summarizes the in-plane dimensions of the waveguide-based test vehicles used for the comparison of the axial mode shape functions [i.e., $\Psi(z)$], extracted from analytical derivations [1] and COMSOL simulations. All the waveguides have a thickness of 20 μm in (100) silicon plate. Considering the small relative thickness of the AlN transducer compared to Si ($\sim$1:40), and to ensure accurate comparison to analytical results presented in [1], AlN piezoelectric stack is not included in the FEM models. Two sets of waveguides aligned to $\langle 110 \rangle$ and $\langle 100 \rangle$ crystal axes are used to compare the effect of crystallographic orientation on the vibration modes for first width-extensional (WE_1) and third width-extensional (WE_3) guided waves, with dispersion types II and I, respectively. Fig. 1 demonstrates the geometry of the waveguides with in-plane dimensions presented in Table I. Besides the waveguides consisting of constituent rectangular regions with abrupt variation in widths [Fig. 1(a)], an alternative geometry created from a gradual variation of the waveguide width is also studied [Fig. 1(b)]. These two configurations are hereafter referred to as abrupt and gradual waveguides, respectively. Fig. 2 shows the vibration mode shape of waveguides operating in the WE_3 guided wave with type-I dispersion, for abrupt and gradual waveguides shown in Fig. 1. These waveguides are hereafter referred to as "type-I waveguides," while waveguides operating in the WE_1 guided wave demonstrating type-II and I-dispersion are referred to as "type-II waveguides," for simplicity. The displacement fields in the x- and z-directions (i.e., U_x and U_z) are shown by the color code, highlighting the acoustic energy distribution over the length of the waveguide. Fig. 3 shows the comparison of the analytical and simulated axial mode shape functions [1] for the type-I waveguides, with abrupt and gradual configurations, operating in the WE_3 cross-sectional vibration pattern. In all the simulations, waveguides are terminated with low-reflectivity boundary condition to avoid destructive reflection of P- and S-waves back into the

TABLE I
Waveguide In-Plane Dimensions

	Region I		Region II		Region III		f_0
	W_1	Z_1	W_2	Z_2	W_3	Z_3	
Type I <110>	114μm	300μm	120μm	100μm	108μm	100μm	108 MHz
Type II <110>	50μm	150μm	52μm	100μm	45μm	100μm	82.9 MHz
Type II <100>	50μm	150μm	56μm	100μm	40μm	100μm	76.5 MHz

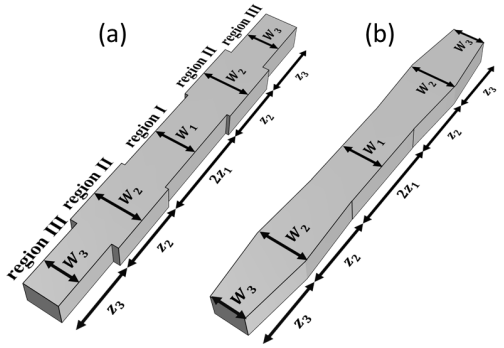

Fig. 1. Two waveguide configurations that are used for acoustic energy localization of type-I and type-II guided waves. (a) Waveguide with abrupt variations in constituent regions, following the design procedure discussed in Part I of this paper. (b) Alternative configuration that replaces abrupt variations/steps with gradually changing width over the waveguide length.

Manuscript received March 18, 2019; accepted April 26, 2019. Date of current version June 5, 2019. This work was supported by the NSF under Grant ECCS 1752206. *(Corresponding author: Mayur Ghatge.)*

The authors are with the Electrical and Computer Engineering Department, University of Florida, Gainesville, FL 32611 USA (e-mail: ruyam@ufl.edu; rtabrizian@ufl.edu).

Digital Object Identifier 10.1109/TUFFC.2019.2914582

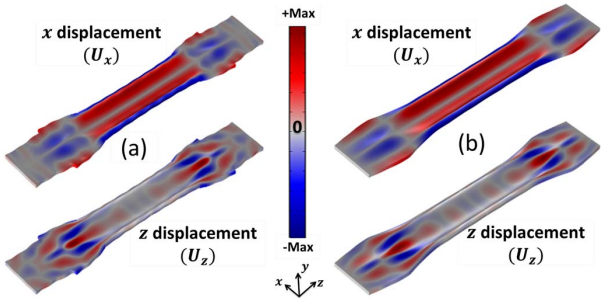

Fig. 2. Vibrational mode shape of the type-I waveguide, operating in the WE_3 mode, for (a) abrupt and (b) gradual waveguides shown in Fig. 1. The color code demonstrates the displacement fields in the x- and z-directions (i.e., U_x and U_z).

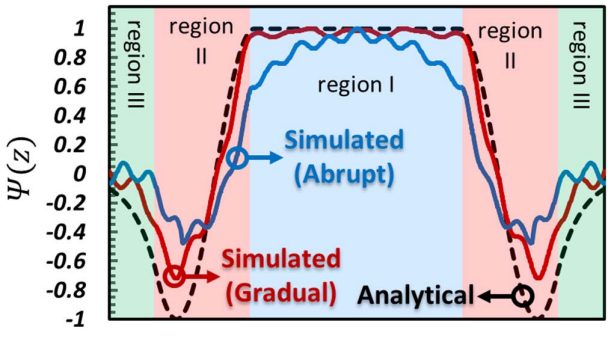

Fig. 3. Analytical and FEM simulated axial mode shape functions for waveguides with type-I dispersion, in abrupt and gradual configurations.

waveguide. The simulated axial mode shape function $\Psi(z)$ is identified through monitoring the particle displacement in an orthogonal direction to the waveguide axis and over an arbitrary cut line parallel to the axis. As evident in Fig. 3, while the acoustic energy localization has been successfully achieved, the simulated $\Psi(z)$ in the abrupt waveguide slightly deviates from the analytical derivation. This can be attributed to the excitation of other guided waves at the same frequency that distorts the wave propagation dynamics beyond the model discussed in the first part of this paper [1]. Such distortion imposes energy distribution gradient in region I of the waveguide, where transduction electrodes are to be placed, thus degrading k_t^2 of the resonator. Alternatively, opting for the gradual configuration, the flatness of the mode shape function in region I can be recovered without distorting the energy trapping efficiency.

Fig. 4 demonstrates the vibration mode shape function of type-II waveguides, operating in WE_1 mode, for abrupt and gradual configurations and aligned to ⟨110⟩ and ⟨100⟩ crystallographic directions in the (100) silicon plane. Fig. 5 shows the comparison of the analytical and FEM-simulated axial mode shape functions $\Psi(z)$ for abrupt and gradual waveguides shown in Fig. 4. While the analytical and simulated axial mode shapes are very close in the case of the waveguide aligned to ⟨110⟩ direction, in ⟨100⟩-aligned waveguide, the abrupt configuration fails to localize the acoustic energy in region I. This can be attributed to the destructive effect of other guided waves that are excited in the waveguide at f_0. Specifically, for the case of WE_1 mode, S_0 waves are excited with the large amplitude and thus get coupled

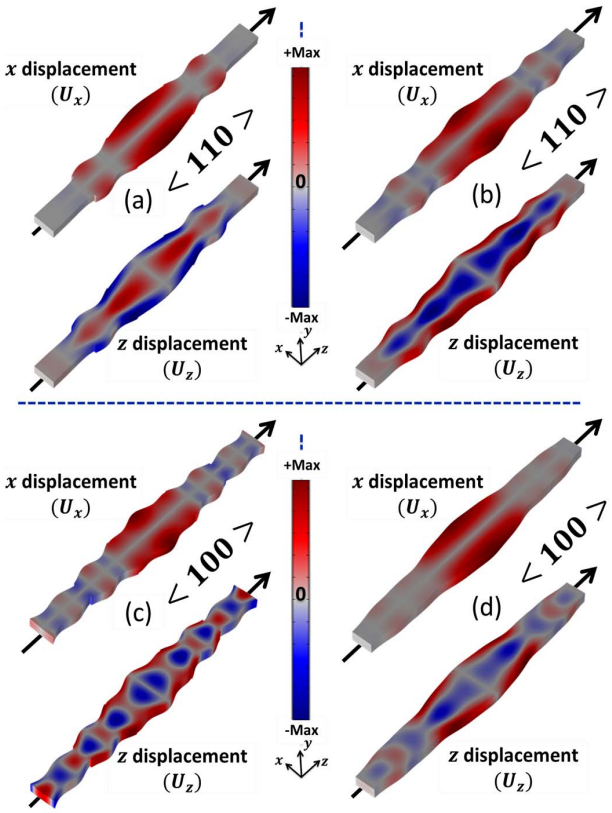

Fig. 4. Vibration mode shapes of type-II waveguides, operating in the WE_1 mode, for (a) and (c) abrupt and (b) and (d) gradual configurations and aligned to (a) and (b) ⟨110⟩ and (c) and (d) ⟨100⟩ crystallographic directions, respectively.

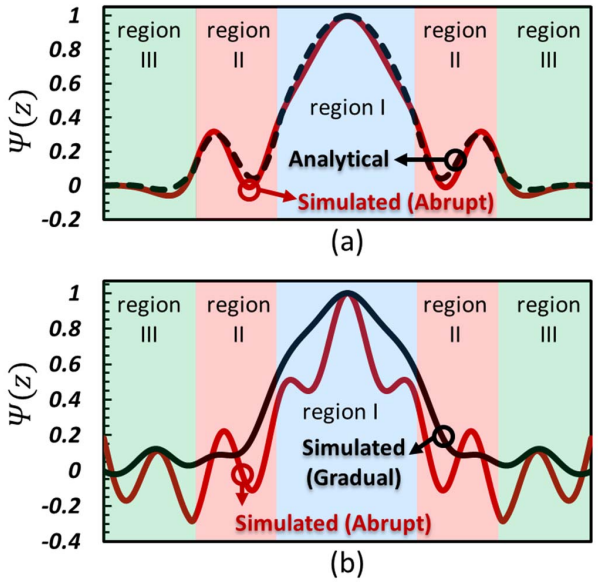

Fig. 5. Analytical and FEM simulated axial mode shape functions for waveguides with type-II dispersion, in abrupt and gradual configurations and aligned to (a) ⟨110⟩ and (b) ⟨100⟩ crystallographic directions of the (100) plane.

to S_1 waves through Poisson's ratio, thus diverging the actual mode shape from analytical design. Considering the significantly larger Poisson's ratio of silicon in ⟨100⟩ direction when compared to ⟨110⟩ [2], the destructive effect of S_0 waves is distinctively pronounced, as shown in Fig. 5.

Although evanescent waves-based energy localization has been demonstrated for S_0 waves [3], its applicability for the design of higher order guided-wave resonators, i.e., WE_1 or WE_3 mode is not possible due to the higher frequency range of operation compared to S_0 evanescent branch. Besides diverging from the analytical design, the excitation of S_0 waves may degrade k_t^2 and Q of the resonator, by distorting the uniform axial mode shape in the active region (region I) of the waveguide and serving as a means for acoustic energy dissipation into the substrate. In order to reduce the energy leakage through S_0 waves, the waveguide terminations can be geometrically engineered to realize acoustic bandgaps around operation frequency f_0 [4]–[7], formation of reflecting mirrors [8], or opting for unparalleled termination surfaces to avoid the formation of S_0-based standing waves with amplified amplitudes [9]. Alternatively, as demonstrated in Fig. 5(b), opting for gradual architecture for ⟨100⟩-aligned waveguides significantly suppresses the undesired S_0 excitations and axial mode shape distortion, thus enabling efficient energy localization in region I. While the reason behind such a significant improvement is not clearly understood, it can be attributed to the change in the dynamics of bulk acoustic wave propagation in waveguides with trapezoid architectures [10].

II. Experimental Demonstration of Dispersion-Engineered Guided Wave Resonators

Two-port dispersion-engineered guided wave resonators are implemented in a silicon-on-insulator (SOI) substrate with 20-μm device layer thickness. The devices are transduced using a 500-nm piezoelectric AlN film deposited on the top surface of the substrate.

A. Fabrication Process

Fig. 6 summarizes the fabrication process used for the implementation of guided wave resonators. The piezoelectric transduction stack consisting of 500-nm AlN film, sandwiched between 50-nm molybdenum (Mo) layers, is deposited using magnetron sputtering. Top Mo layer is patterned to create drive and sense transduction ports in the central region (i.e., region I) of the waveguides. This is followed by patterning the AlN film to accommodate access to the bottom Mo layer, which serves as the common ground for the two-port transduction scheme. The lateral geometry of the waveguides is then patterned through etching trenches in AlN, bottom Mo, and Si device layers. The reactive ion etching (RIE) process used for AlN patterning is optimized to ensure the straight sidewall of the film after etching. The silicon layer is etched through the Bosch deep reactive ion etching process optimized to reduce the size of scallops and ensure straight sidewall across the device thickness. Fig. 7 demonstrates the two-port guided wave resonators fabricated in AlN-on-Si platform and aligned to ⟨110⟩ and ⟨100⟩ crystallographic directions.

B. Device Characterization

The two-port resonators are characterized at room temperature using a Keysight N5242 performance network analyzer. Fig. 8(a) demonstrates the frequency response of the type-I

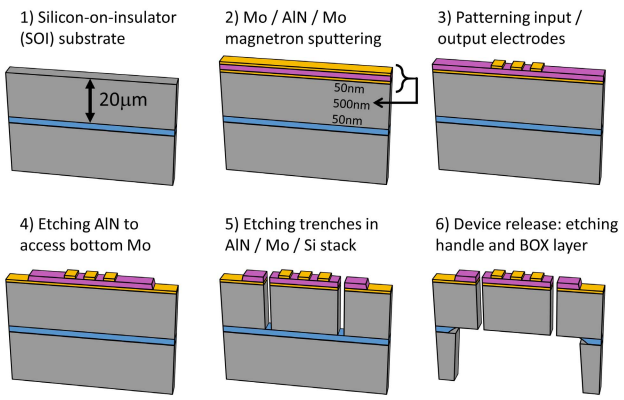

Fig. 6. Fabrication process for the implementation of type-I and type-II waveguides in the AlN-on-Si substrate.

abrupt waveguides over 20–120 MHz span. The WE_3 mode is evident at 108.7 MHz with Q of 2400. Besides this mode of interest, the frequency response shows another mode at 54.2 MHz with Q of 1195, which corresponds to the guided wave with an out-of-plane flexural cross-sectional mode shape. Fig. 8(b) shows the frequency response of type-I gradual waveguide over 20–120 MHz span. Besides the two modes at ∼54 and ∼108 MHz, the large span frequency response demonstrates the excitation of several spurious modes, which can be attributed to the expansion of solution space in gradual waveguide compared to the abrupt counterpart. Despite the increased number of spurious modes, the gradual waveguide architecture demonstrates a significant improvement in energy trapping efficiency through an increase in Q and decrease in insertion loss (IL). Fig. 8(c) and (d) shows the comparison of the short-span frequency response of the abrupt and gradual waveguides around the flexural and WE_3 modes at ∼54 and ∼108 MHz, respectively. For the mode of interest (i.e., WE_3), Q is improved to 4482, which is nearly two times larger compared to its abrupt counterpart. Furthermore, the IL of the gradual waveguide is ∼13 dB lower compared to the abrupt waveguide, which corresponds well with the improvement in the uniformity of axial mode shape function (Fig. 3) in the electrode region (i.e., region I) of the waveguide. Q can be further enhanced by opting longer energy decaying length for region III.

Fig. 9(a) and (c) demonstrates the frequency response of type-II abrupt waveguide aligned to ⟨110⟩ crystallographic direction [Fig. 7(c)]. A high Q of ∼19 000 is measured at 82 MHz, with an IL of −23.4 dB, showing the effectiveness of dispersion engineering for acoustic energy localization using the propagating-evanescent wave in region III. Fig. 9(b) and (d) shows the frequency response of type-II gradual waveguide aligned to ⟨100⟩ crystallographic direction [Fig. 7(d)]. A high Q of 13 000 is measured at 76 MHz with IL of −20 dB.

III. Experimental Verification of Analytical Mode Synthesis in Type-II Waveguide

To verify the effectiveness of the analytical mode synthesis, experimental test vehicles are implemented in AlN-on-Si platform to identify the contribution of regions II and III on

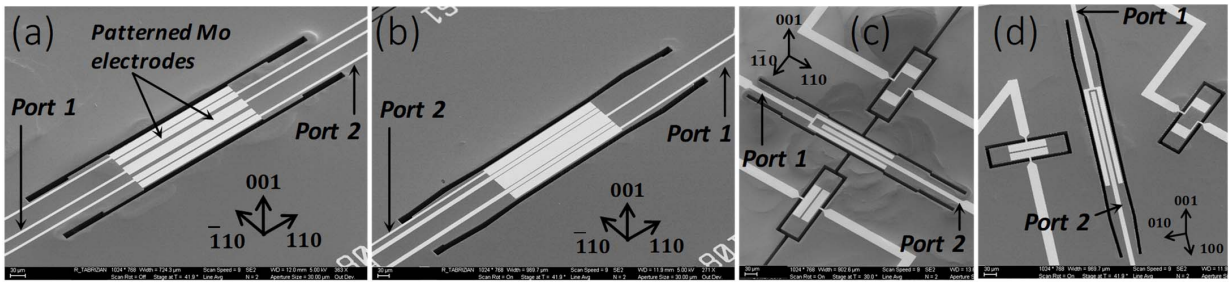

Fig. 7. SEM image of the fabricated devices in AlN-on-Si substrate: type I ⟨110⟩-aligned (a) abrupt and (b) gradual waveguides and type II (c) ⟨110⟩-aligned abrupt and (d) ⟨100⟩-aligned gradual waveguides.

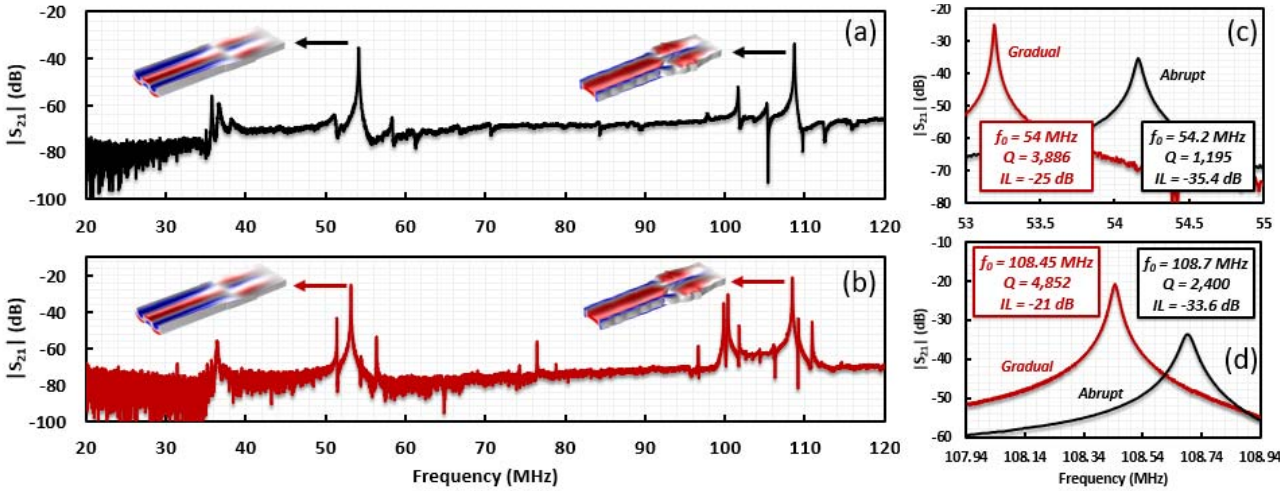

Fig. 8. Measured frequency response of type-I waveguides. (a) Large-span response of the abrupt waveguide. (b) Large-span response of the gradual waveguide. Short-span response around (c) flexural and (d) WE_3 modes for abrupt and gradual waveguides.

the energy localization of WE_1 guided waves with type-II dispersion. Fig. 10(a)–(c) demonstrates the three test vehicles implemented in AlN-on-Si substrate with 20-μm device layer thickness. All the devices are aligned to ⟨110⟩ crystallographic orientation. Waveguide 3 is analytically engineered to localize the acoustic energy in region I, through standing- and propagating-evanescent waves in regions II and III, respectively. Waveguides 1 and 2 are similar to waveguide 3, except missing one or both of regions II and III. The comparison of these test vehicles enables the identification of the significance of regions II and III for high-Q acoustic energy localization.

The top Mo electrodes are identically patterned on all three waveguides [i.e., Fig. 10(a)–(c)] and enable two-port characterization of frequency responses. Fig. 11 shows the comparison of the measured frequency response of waveguides 1–3 over a 10-MHz span around the WE_1 resonance mode at 82 MHz. While a high Q of ∼19 000 is measured for the waveguide with all three regions (i.e., waveguide 3 in Fig. 10), waveguides 1 and 2 are not capable of efficient energy localization. Among these, for waveguide 1 [i.e., Fig. 10(a)], COMSOL simulations anticipate the formation of a standing wave by geometrical suspension through anchoring region I at the terminal faces. However, in practice, such a fixed boundary condition is not realized due to the acoustic coupling of guided waves into the substrate that depletes the energy out of the waveguide. The addition of region II, which supports standing evanescent at f_0, slightly improves the energy localization in waveguide 2. However, small wavenumbers of the excited standing-evanescent wave and the finite length of region II prevent sufficient attenuation of the axial mode function, hence preventing from high-Q energy localization at the resonance mode. Finally, the addition of region III, which supports propagating-evanescent wave at excitation frequency (82 MHz), further attenuates the axial mode shape amplitude and provides nodal points for perfect anchoring of waveguide 1, thus yielding a high Q.

Besides enabling high-Q energy trapping, analytical mode engineering is highly effective in suppression of spurious modes. Fig. 12 shows the comparison of the frequency response of a rectangular silicon bulk acoustic resonator (SiBAR) anchored to the substrate through narrow tethers, with an analytically engineered waveguide. The width of the SiBAR is identical to the width of region I in the type-II dispersion-engineered waveguide. The length of the two devices and the electrode configurations are kept identical to enable a precise comparison of the two design strategies. While the SiBAR suffers from various spurious modes in the 10-MHz frequency span around the WE_1 mode at ∼82 MHz, the engineered waveguide demonstrates a clean frequency response with a single high-Q resonance peak and significantly suppressed spurious modes. Such spurious suppression as a result of analytical engineering for a specific solution in abrupt waveguide architecture is not necessarily suitable for energy trapping of spurious modes. Therefore, while anchoring of the

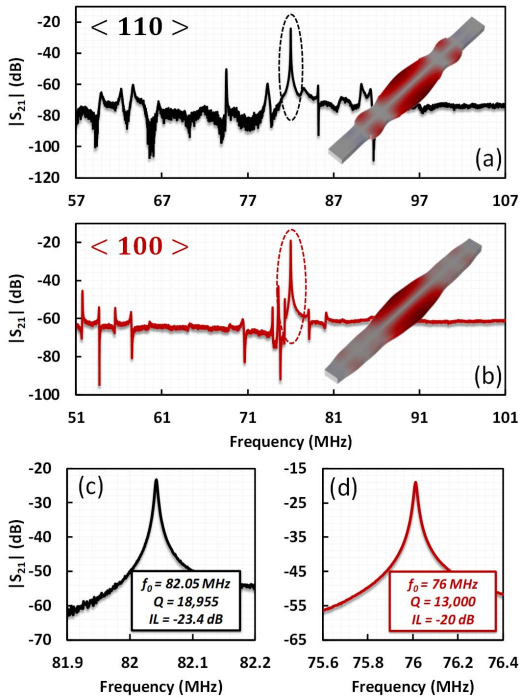

Fig. 9. Measured frequency response of the type-II waveguides. (a) Large-span response of the abrupt waveguide aligned to ⟨110⟩. (b) Large-span response for the gradual waveguide aligned to ⟨100⟩. Short-span frequency response of (c) ⟨110⟩-aligned abrupt and (d) ⟨100⟩-aligned gradual waveguides around WE_1 mode.

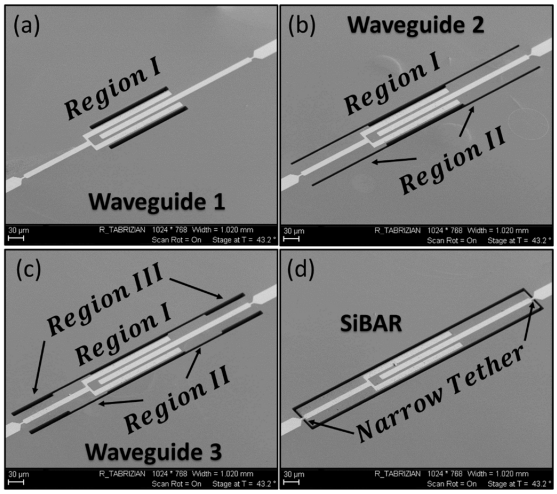

Fig. 10. (a)–(c) SEM image of test vehicles implemented for the verification of the effect of constituent regions in type-II abrupt waveguide and comparison with (d) SiBAR anchored to the substrate through narrow tethers. All devices are aligned to ⟨110⟩ crystallographic direction.

engineered waveguide to the substrate using the wide tether (i.e., region III) does not affect Q of the synthesized mode, it provides a mean for energy leakage of the spurious modes out of the device. This is clearly not the case for the rectangular SiBAR that is surrounded by stress-free boundaries, which blindly trap all spurious modes in the device. Extensive simulation-based design optimization can be carried out to design SiBAR with suppressed spurious modes, but this lacks systematic analytical design methodology like the proposed dispersion-engineered waveguide-based resonators.

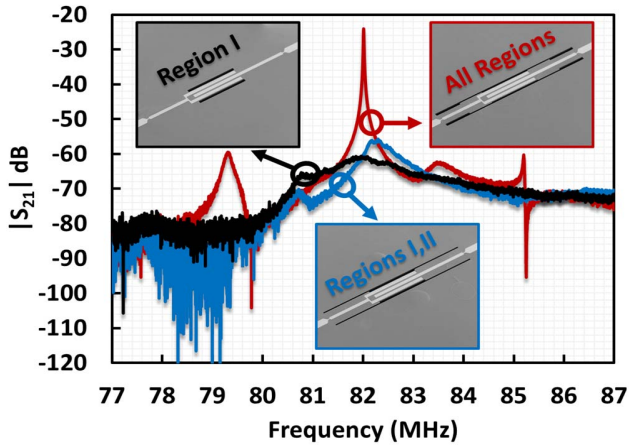

Fig. 11. Measured frequency response of waveguides 1–3 shown in Fig. 10(a)–(c), highlighting the effect of regions II and III for high-Q energy localization of the WE_1 mode, with type-II dispersion, at ~82 MHz.

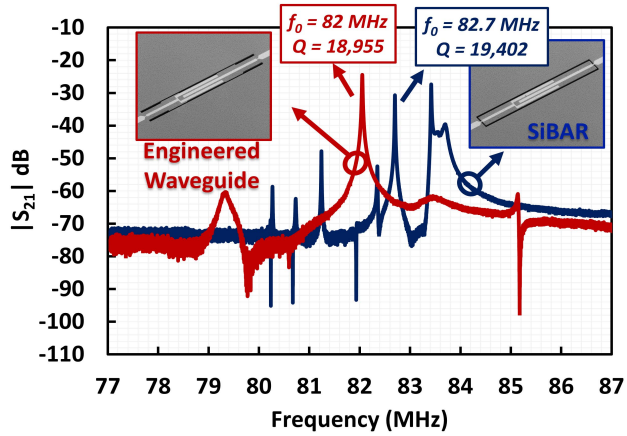

Fig. 12. Measured frequency response of the type-II dispersion-engineered waveguide in comparison with a SiBAR that is anchored to the substrate by two narrow tethers.

Finally, to verify the repeatability of the presented analytical resonator design procedure, various type-I and type-II resonators, randomly chosen across the 100-mm substrate, are characterized. A group of 20 type-I and 30 type-II resonators are used for the verification of performance repeatability. Fig. 13(a) and (c) shows the comparison of the frequency response of various resonators out of the randomly chosen samples to compare the frequency response and spurious mode distribution for type-I and type-II resonators. It is evident that the fabrication imperfections result in slight changes in frequency response and spurious mode generation. Specifically, lithographical uncertainties induce undesired and randomly distributed variations in device lateral dimensions, which directly affect the dispersion characteristic of constituent waveguides. Such variations result in fluctuations in analytically synthesized mode shapes and affect the geometrical energy-distribution profile and resonator Q. Fig. 13(b) and (d) demonstrates the frequency and Q distribution of the type-I and type-II resonators, highlighting a consistent performance across the sample groups. Further improvement in performance repeatability requires the use of process compensation techniques [11], [12] to suppress the effect of geometrical variations in resonator performance.

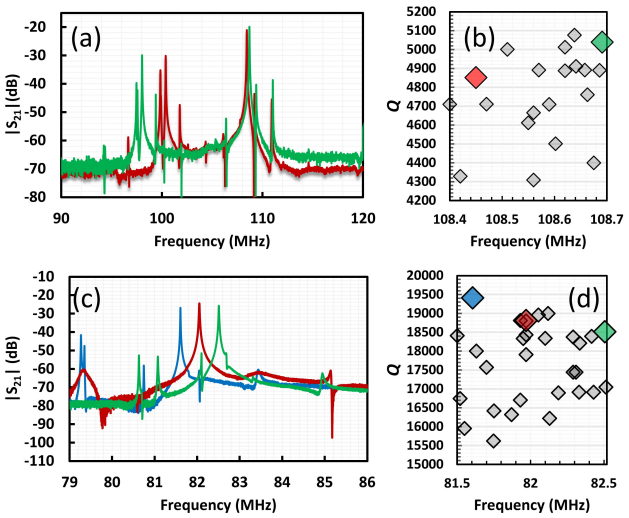

Fig. 13. Comparison of resonator performance across the wafer. (a) Frequency response of two type-I resonators. (b) Frequency-Q distribution of 20 type-I resonators. (c) Frequency response of three type-II resonators. (d) Frequency-Q distribution of 30 type-I resonators.

IV. Conclusion

This paper presents an analytical approach for designing high-Q guided wave resonators in single-crystal substrates. The design procedure is based on the analytical extraction of dispersion characteristic of guided waves with arbitrary in-plane cross-sectional vibration patterns in rectangular waveguides aligned to the arbitrary crystallographic direction. Various types of guided waves with a similar cross-sectional mode vibration pattern but different spatial dynamics are identified consisting of propagating, standing-evanescent, and propagating-evanescent waves. These waves are used to synthesize high-Q vibration modes through the acoustic coupling of waveguides with different cross-sectional dimensions. Two types of guided waves with type-I and type-II dispersion characteristics are identified, and the design procedures for both types are presented.

The effectiveness of the analytical mode synthesis is verified through the finite-element simulation of type-I and type-II guided wave resonators in various crystallographic orientations of the single-crystal silicon substrate. The discrepancies between the analytical mode shape functions and simulations are discussed, and a geometrical approach to minimize them is introduced. Proof-of-concept two-port guided wave resonators are implemented in AlN-on-Si platform and characterized to confirm the capability of the analytical design procedure for the realization of high-Q type-I and type-II resonators. Finally, various test vehicles are implemented to experimentally identify the effectiveness of the analytical mode synthesis approach and its capability for spurious mode suppression.

References

[1] M. Ghatge and R. Tabrizian, "Dispersion-engineered guided-wave resonators in anisotropic single-crystal substrates—Part I: Concept and analytical design," *IEEE Trans. Ultrason., Ferroelectr., Freq. Control*, vol. 66, no. 6, pp. 1140–1148, Jun. 2019.

[2] J. J. Wortman and R. A. Evans, "Young's modulus, shear modulus, and Poisson's ratio in silicon and germanium," *J. Appl. Phys.*, vol. 36, no. 1, pp. 153–156, Jan. 1965.

[3] B. Abbott *et al.*, "Temperature compensated SAW with high quality factor," in *Proc. IEEE Int. Ultrason. Symp. (IUS)*, Sep. 2017, p. 1.

[4] L. Sorenson, J. L. Fu, and F. Ayazi, "One-dimensional linear acoustic bandgap structures for performance enhancement of AlN-on-Silicon micromechanical resonators," in *Proc. 16th Int. Solid-State Sensors, Actuat. Microsystems Conf.*, Jun. 2011, pp. 918–921.

[5] C.-M. Lin, J.-C. Hsu, D. G. Senesky, and A. P. Pisano, "Anchor loss reduction in ALN Lamb wave resonators using phononic crystal strip tethers," in *Proc. IEEE Int. Freq. Control Symp. (FCS)*, May 2014, pp. 1–5.

[6] F.-C. Hsu, J.-C. Hsu, T.-C. Huang, C.-H. Wang, and P. Chang, "Reducing support loss in micromechanical ring resonators using phononic band-gap structures," *J. Phys. D, Appl. Phys.*, vol. 44, no. 37, Aug. 2011, Art. no. 375101.

[7] H. Zhu and J. E. Lee, "Design of phononic crystal tethers for frequency-selective quality factor enhancement in AlN piezoelectric-on-silicon resonators," *Procedia Eng.*, vol. 120, pp. 516–519, Jan. 2015.

[8] B. P. Harrington and R. Abdolvand, "Journal of Micromechanics and Microengineering in-plane acoustic reflectors for reducing effective anchor loss in lateral–extensional MEMS resonators," *J. Micromech. Microeng.*, vol. 21, no. 8, Jul. 2011, Art. no. 085021.

[9] J. E.-Y. Lee, J. Yan, and A. A. Seshia, "Study of lateral mode SOI-MEMS resonators for reduced anchor loss," *J. Micromech. Microeng.*, vol. 21, no. 4, Mar. 2011, Art. no. 045010.

[10] K. F. Graff, *Wave Motion In Elastic Solids*. Chelmsford, MA, USA: Courier Corporation, 2012.

[11] G. K. Ho, J. K. Perng, and F. Ayazi, "Micromechanical IBARs: Modeling and process compensation," *J. Microelectromech. Syst.*, vol. 19, no. 3, pp. 516–525, Jun. 2010.

[12] F. Ayazi, R. Tabrizian, and L. Sorenson, "Compensation, tuning, and trimming of MEMS resonators," in *Proc. IEEE Int. Freq. Control Symp.*, May 2012, pp. 1–7.

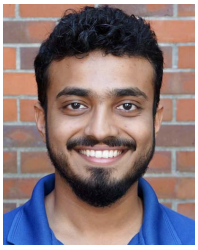

Mayur Ghatge (S'17) received the bachelor's degree in electrical engineering from IIT Jodhpur, Jodhpur, India, in 2014. He is currently pursuing the Ph.D. degree with the Department of Electrical and Computer Engineering, University of Florida, Gainesville, FL, USA.

From 2014 to 2015, he was a Research Assistant at the Indian Institute of Science, Bengaluru, India. His current research interests include linear and nonlinear RF MEMS and microfabrication/nanofabrication technologies.

Mehrdad Ramezani (S'17) received the B.S. degree in electrical engineering from the Sharif University of Technology, Tehran, Iran, in 2016. He is currently pursuing the Ph.D. degree with the Department of Electrical and Computer Engineering, University of Florida, Gainesville, FL, USA.

His research focuses on development of novel fin-based nanoacoustic resonators for RF spectral processing applications.

Roozbeh Tabrizian (S'06–M'14) received the B.S. degree in electrical engineering from the Sharif University of Technology, Tehran, Iran, in 2007 and the Ph.D. degree in electrical and computer engineering from the Georgia Institute of Technology, Atlanta, GA, USA, 2013.

From 2014 to 2015, he was a Post-Doctoral Scholar at the University of Michigan, Ann Arbor, MI, USA. He is currently an Assistant Professor with the Department of Electrical and Computer Engineering, University of Florida, Gainesville, FL, USA. His current research interests include linear and nonlinear microacoustic and nanoacoustic devices, RF MEMS, mixed-domain nanosystems for time-keeping and transfer, frequency reference, and spectroscopy applications, and nanofabrication technologies. His research has resulted in more than 40 journal and refereed conference papers. He holds 16 patents and patent applications.

Dr. Tabrizian and his students are recipients of Outstanding Paper Awards at the IEEE International Conference on Micro Electro Mechanical Systems (IEEE MEMS) and the International Conference on Solid-State Sensors, Actuators, and Microsystems (Transducers).